USING DESIGN OF EXPERIMENTS IN FINITE ELEMENT MODELING TO IDENTIFY CRITICAL VARIABLES FOR LASER POWDER BED FUSION

Li Ma, Jeffrey Fong, Brandon Lane, Shawn Moylan, James Filliben, Alan Heckert, and Lyle Levine

National Institute of Standards and Technology, 100 Bureau Drive, Gaithersburg, MD 20899
REVIEWED

Abstract

Input of accurate material and simulation parameters is critical for accurate predictions in Laser Powder Bed Fusion (L-PBF) Finite Element Analysis (FEA). It is challenging and resource consuming to run experiments that measure and control all possible material properties and process parameters. In this research, we developed a 3-dimensional thermal L-PBF FEA model for a single track laser scan on one layer of metal powder above a solid metal substrate. We applied a design of experiments (DOE) approach which varies simulation parameters to identify critical variables in L-PBF. DOE is an exploratory tool for examining a large number of factors and alternative modeling approaches. It also determines which approaches can best predict L-PBF process performance.

1. Introduction

Laser powder bed fusion (L-PBF) is an additive manufacturing (AM) technology for the fabrication of near net shaped parts directly from computer-aided design (CAD) data by sequentially melting layers of metal powder with a laser source. L-PBF is one of the most promising additive manufacturing processes because it provides better surface and geometric part quality compared to other metal AM technologies. However, the highly localized laser power input leads to extremely high local temperature gradients. As a result, significant residual stresses, distortion, unique microstructures, and defects may occur within a workpiece. A round robin comparison of mechanical properties [1] found that the quality and properties of deposits can vary significantly even when all producers are using the same materials, processing parameters, and, in some cases, even when the same type of L-PBF machine is used.

L-PBF finite element modeling plays an important role in understanding the L-PBF process, predicting optimal fabrication strategies, and qualifying fabricated parts based on those strategies. Accurate temperature prediction from computational thermal modeling is also critical for modeling microstructure evolution and residual stresses. Although several thermal finite element analysis (FEA) models appear in the literature [2-14], significant challenges remain to construction of accurate FEA simulations of the L-PBF process. Input of accurate material and simulation parameters is critical for accurate prediction of process signatures, such as peak temperature, melting pool size, etc. The measurement and control of all possible material properties and processing parameters is challenging and resource consuming. Therefore, a computational design of experiments (DOE) approach was undertaken to simplify this task.

In this research, we developed 3-dimensional thermal FEA models of L-PBF process. These FEA L-PBF thermal models incorporate a continuous moving heat source, phase changes, and powder thermal property changes after melting. A single track laser scan on one layer of metal powder above a solid metal substrate was modeled. A computational DOE approach was used that varied simulation parameters to identify the critical variables for accurate representation of the L-PBF process.

2. Computational Design of Experiments

As discussed above, to explore the dominant factors contributing to the uncertainty of the L-PBF process, we applied a computational DOE approach. The results from the FEA models with a range of processing parameters and materials properties provide the evaluation input for the DOE.

2.1. Model description

Using the commercial FEA code ABAQUS[1] [15], a non-linear, transient, thermal model was designed and executed to obtain the global temperature history generated during a single AM laser scan. The mesh design is shown in Fig. 1. The specimen is a solid substrate with one layer of powder. The dimensions of the specimen are 6 mm (length) × 1.4 mm (width) × 0.6 mm (thickness). The powder layer thickness is 37 μm. A single-track laser scan across the metal powder layer was modeled. To reduce computation time, the elements that interact with the laser beam are finely meshed with six hexahedral elements within the diameter of the laser, and a coarse mesh is used for the surrounding loose powder and substrate. Within the fine mesh, the element size is 16.7 μm (length) × 16.7 μm (width) × 12.3 μm (thickness).

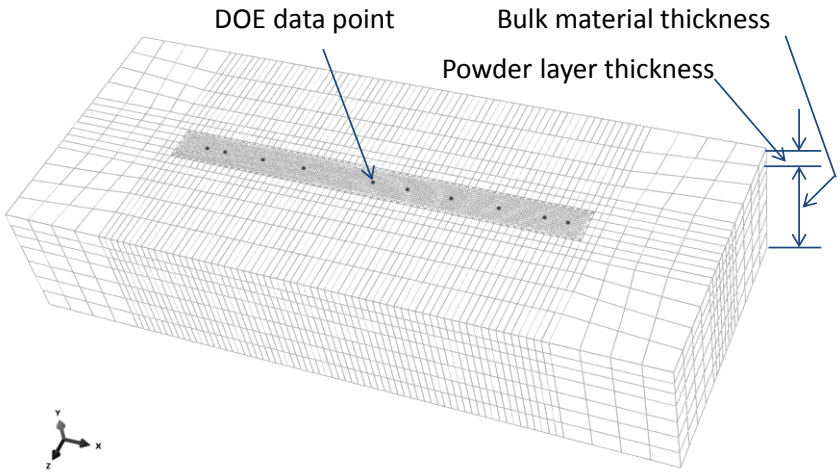

Figure1: Finite element one track thermal model mesh. The dark dots are the points used for the temperature history output.

[1] Certain commercial entities, equipment, or materials may be identified in this document in order to describe an experimental procedure or concept adequately. Such identification is not intended to imply recommendation or endorsement by the National Institute of Standards and Technology, nor is it intended to imply that the entities, materials, or equipment are necessarily the best available for the purpose.

2.2. Thermal modeling

The heat conduction in the L-PBF process was modeled using the Fourier heat conduction equation given by Carslaw and Jaeger [16]:

$$\rho c \frac{\partial T}{\partial t} = \frac{\partial}{\partial x}\left(k \frac{\partial T}{\partial x}\right) + \frac{\partial}{\partial y}\left(k \frac{\partial T}{\partial y}\right) + \frac{\partial}{\partial z}\left(k \frac{\partial T}{\partial z}\right) + Q \quad (1)$$

where ρ is the material density; c is the specific heat capacity; k is the thermal conductivity; T is the temperature; t is the interaction time, and Q is the internal heat.

The initial condition assumed a uniform temperature distribution throughout the specimen at time $t = 0$, which can be expressed as

$$T(x, y, z, 0) = T_0 \quad (2)$$

where T_0 is the preheat temperature taken as 353 K (80 °C).

The boundary condition on the top surface includes the input heat flux, surface convection, and radiation that follow the equation:

$$(-k\nabla T) \cdot \hat{n} = q_s + h(T - T_e) + \varepsilon_\theta \sigma\left(T^4 - {T_e}^4\right) \quad (3)$$

where q_s represents the laser heat input, h is the convection heat transfer coefficient, ε_θ is the thermal radiation coefficient, σ is the Stefan-Boltzmann constant, and T_e is the ambient temperature. An adiabatic boundary condition was applied to all the surfaces except the top surface of the specimen.

2.4. Modeling the moving heat flux

The laser in this study is the continuous Ytterbium fiber diode laser (wavelength = 1.064 μm) that is widely used in actual L-PBF processes. A user subroutine was developed to simulate the characteristics of the heat flux of the laser onto the sample surface. The surface heat flux of the laser beam is modeled as a Gaussian distribution [7]:

$$q_s = \frac{2AP}{\pi r_b} exp\left(\frac{-2r^2}{r_b^2}\right), \quad (4)$$

where P is the laser power, A is the absorption coefficient of the powder layer, r is the radial distance relative to the center of laser beam, and r_b is the radius of the laser beam, which is 50 μm in our simulations.

2.5. Materials properties

Inconel 625 was used in this study because: a) it is widely used in the L-PBF process, and b) it was the material used in the L-BPF round robin tests [1].

The powder packing ratio, φ, is a function of the local density of the powder, ρ_{powder}, and the density of the solid material, ρ_{bulk}:

$$\varphi = \frac{\rho_{powder}}{\rho_{bulk}}. \quad (5)$$

In our FEA model, the initial powder density linearly increases to the bulk density when the temperature is above the solidus temperature, T_s, and below the liquidus temperature, T_l, on the Inconel 625 phase diagram [20, 21]. The initial powder-state elements are irreversibly changed to bulk-state elements when the temperature exceeds T_l. Consequently, the density and thermal conductivity of the powder bed are treated as a function of temperature and a melt-state variable which records if the powder has experienced the first melting point. These changes are performed by the ABAQUS user subroutine and ρ_{powder} is defined as:

$$\rho_{powder} = \begin{cases} \varphi\rho_{bulk}(T), \ \ T \le T_s, \ \ Before\ first\ melt \\ \varphi\rho_{bulk}(T_s) + \frac{\rho_{bulk}(T_s) - \varphi\rho_{bulk}(T_s)}{T_l - T_s}(T - T_s), \ \ T_l < T < T_s, \ \ First\ melt. \\ \rho_{bulk}(T), \ \ T \ge T_l, \ \ First\ melt \\ \rho_{bulk}(T), \ \ After\ first\ melt \end{cases} \quad (6)$$

From prior research [17, 18], the effective thermal conductivity of a powder bed depends not only on the conductivity of the bulk material, but also on the packing fraction, the particle size distribution, the particle morphology, and the thermal conductivity of the surrounding gas. It was found that the thermal conductivity of the powder, k_{powder}, is much smaller than that of the bulk material at room temperature [17]. In these simulations, the thermal conductivity of the powder is not directly connected to the powder packing ratio and $k_{powder}(T)$ ranged from 1.0 W/mK to 3.0 W/mK [19] before the first melt. The effective thermal conductivity of the powder $k_{powder,eff}$ is defined as

$$k_{powder,eff} = \begin{cases} k_{powder}(T), \ \ T \le T_s, \ \ Before\ first\ melt \\ k_{powder}(T_s) + \frac{k_{bulk}(T_s) - k_{powder}(T_s)}{T_l - T_s}(T - T_s), \ \ T_l < T < T_s, \ \ First\ melt. \\ k_{bulk}(T), \ \ T \ge T_l, \ \ First\ melt \\ k_{bulk}(T), \ \ After\ first\ melt \end{cases} \quad (7)$$

where k_{bulk} is the thermal conductivity of the bulk material. The latent heat was added when the temperature was between the solidus and liquidus temperatures. The temperature-dependent bulk material density and specific heat were calculated from a Scheil simulation for the nominal IN625 composition and using the TCNI6 thermodynamic database [20] within the Thermo-Calc software [21].

2.6. Design of experiments

In the L-PBF process, there are dozens of factors that may influence the quality of a final manufactured part [22]. It is challenging and expensive to measure and control all possible material properties and process parameters. For example, if 50 different factors interact with

each other, a proper uncertainty budget should consider, at least, the roughly 1200 2-term interactions as well as the nearly 20,000 3-term interactions formed from combinations of the original 50 parameters. Investigating all of these interactions experimentally is unfeasible. The task of determining the importance of such a large number of factors can be greatly simplified by using *a priori* knowledge of the processing, experimental experience, computation modeling experience, and statistical/computational DOE methods.

To demonstrate this approach, ten factors thought to be important were selected for DOE analysis. These ten factors include both processing and material properties parameters. The choice of factors is guided by prior research, experience on processing quality control, and computational modeling. An exhaustive screening design would likely consider many more factors and a corresponding increase in the number of simulation runs. Since the goal of this preliminary work is to identify dominant factors, and not to fully characterize the response function, we choose a two-level screening design. As the ranges of most factors in the L-PBF process are not available, the values of the two levels (high and low, or + and -) for each of the factors come from our experience, just for demonstration.

The factor and level combinations needed for the screening were drawn from standard tables [23]. In this case, $2_{III}^{(10-6)}$ fractional factorial design was chosen. In this notation, the '2' indicates a two-level design (two possible values for each input parameter), the "10" indicates that ten factors or parameters are considered and the "*III*" reveals that this design is resolution three, which means that the main effects of the ten variables are not confounded with any 2-term interactions. Some confounding of 2-term interactions with each other is present, however. This design requires $2^{(10-6)} = 2^4 = 16$ simulation runs. Table 1 listed the input parameters for the 16 runs used in this research.

Table1: List of input parameters and a resolution III fractional factorial orthogonal design for a 10-factor, 16-run numerical FEM experiment

	X1	X2	X3	X4	X5	X6	X7	X8	X9	X10
Factor Symbol	*E*	*hc*	*Ti*	*Ab*	*Rho*	*Cp*	*k*	*Dp*	*P*	*v*
Factor Meaning	Emmisivity	Convection	Preheat Temperature	Absorption	Density	Specific heat	Thermal Conductivity	Powder Packing Ratio	Laser Power	Scanning Speed
Base Run (00)	0.37	0.05	353	0.12	*Rho (T)*	*Cp (T)*	*k (T)*	50	195	800
Factor Unit		*W/K/m^2*	*K*		*kg/mm^3*	*J/kgK*	*W/mK*	*%*	*W*	*mm/s*
+/- variation	10%	10%	1%	0.5%	1%	3%	3%	10%	2.5%	1.5%
Run No.(01)	-	-	-	-	-	-	-	-	+	+
Run No.(02)	+	-	-	-	+	-	+	+	-	-
Run No.(03)	-	+	-	-	+	+	-	+	-	-
Run No.(04)	+	+	-	-	-	+	+	-	+	+
Run No.(05)	-	-	+	-	+	+	+	-	-	+
Run No.(06)	+	-	+	-	-	+	-	+	+	-
Run No.(07)	-	+	+	-	-	-	+	+	+	-
Run No.(08)	+	+	+	-	+	-	-	-	-	+
Run No.(09)	-	-	-	+	-	+	+	+	-	+
Run No.(10)	+	-	-	+	+	+	-	-	+	-
Run No.(11)	-	+	-	+	+	-	+	-	+	-
Run No.(12)	+	+	-	+	-	-	-	+	-	+
Run No.(13)	-	-	+	+	+	-	-	+	+	+
Run No.(14)	+	-	+	+	-	-	+	-	-	-
Run No.(15)	-	+	+	+	-	+	-	-	-	-
Run No.(16)	+	+	+	+	+	+	+	+	+	+

We note that a k-factor, 2-level orthogonal design, such as the one used in this study, has a balanced number of settings for each factor, and for every pair of factors. Such balance yields many advantages, including: 1) coverage and robustness: the design points provide coverage across the entire k-space of factors, thus yielding robust effect estimates with minimal bias; 2) uncertainty-reduction: each factor effect estimate uses all n observations, thus making the uncertainty for each estimate is as small as possible; 3) superiority over 1-factor-at-a-time experiments: orthogonal designs minimize factor confounding/contamination and maximize (if possible) the ability to estimate interactions; 4) hypothesis testing: if a factor is in fact significant in reality, then our ability to carry out a hypothesis test and conclude the factor is "significant" is maximized; and 5) simplified least squares: the resulting factor effect estimates are least squares equivalent and simplify to (average Y at high setting) – (average Y at low setting).

3. Results

3.1. FEA temperature profile

Figure 2 shows the center point on the scan surface (as shown in Fig. 1) temperature as a function of time for all 16 computational DOE runs. It can be seen that the temperature profile shows a clear transition between the solidus and liquidus temperatures because of the latent heat. For simplicity in this first attempt, we selected the peak temperature of each profile as the DOE input data. In the future, the geometry of the melt pool can be used for a more physically useful parameter.

3.2. Design of Experiments Result

From the FEA model of a single laser scan track using the parameters specified in Table 1 for each of the 16 runs, we obtained the peak temperature at the center point of the specimen top surface during the scanning process. We then conducted a sensitivity analysis using these 16 runs plus a center point (the base design solution) computational experiment, using a computer code written in DATAPLOT [24].

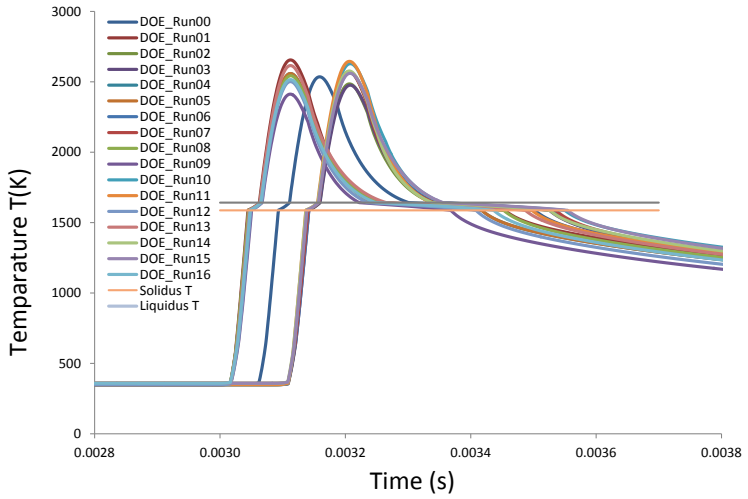

Figure 2: The temperature at the center point of the scan surface (as shown in Fig. 1) as a function of time for all 16 computational DOE runs.

3.2.1 Effects order

One useful tool for quickly visualizing dominant factors is to plot the main effect as shown in Figure 3. When displayed in this format, factors that have a large impact on the peak temperature appear as line segments with large slope. The slope directions denote the peak temperature change direction with the individual factors. In Fig. 3, we observed that the laser power (X9) and material specific heat (X6) have the largest effects, with the laser power being statistically significant at the 95 % percent level. As expected, increasing the laser power will increase the peak temperature while the materials with higher specific heat will generate lower peak temperature.

Figure 4 displays the order of the ten factors affecting the peak temperature. It can be seen that besides laser power (X9) and specific heat (X6), the other dominant factors include the laser scan speed (X10) and the powder packing ratio (X8). Each of these four factors produces a temperature response ≥ 2 %. Lower response factors (≈ 1 %) include the thermal conductivity (X7) and density (X5). Convection has the least impact on the peak temperature.

3.3.3. Significance and limitations of the computational DOE approach as a tool for identifying critical variables in L-PBF

DOE-based sensitivity analysis can play an important role in quality control for additive manufacturing of parts. However, this approach is limited in the sense that it requires the user to exercise judgement in selecting the appropriate number of the parameters for implementation. In case of doubt, one can, nevertheless, try several schemes to obtain reasonable results.

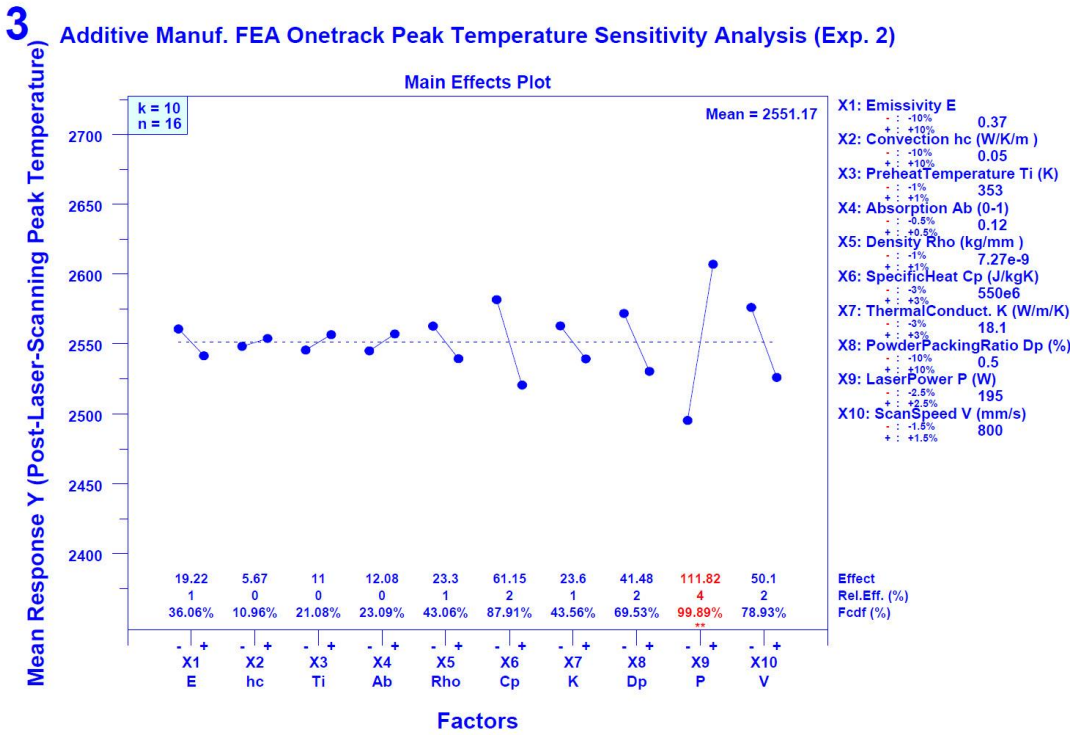

Figure 3: Main effects plot of the 10-factor, 16-run 2-level, fractional factorial orthogonal DOE.

Meanwhile, the current preliminary thermal modeling neglects important factors such as the powder shape and geometry, shrinkage, liquid solid interactions, the dependence of powder thermal conductivity on the powder packing ratio, etc. Also, the processes of vaporization and splattering were neglected. Eventually, all of these factors must be evaluated to determine their role in producing reliable and consistent AM-manufactured parts.

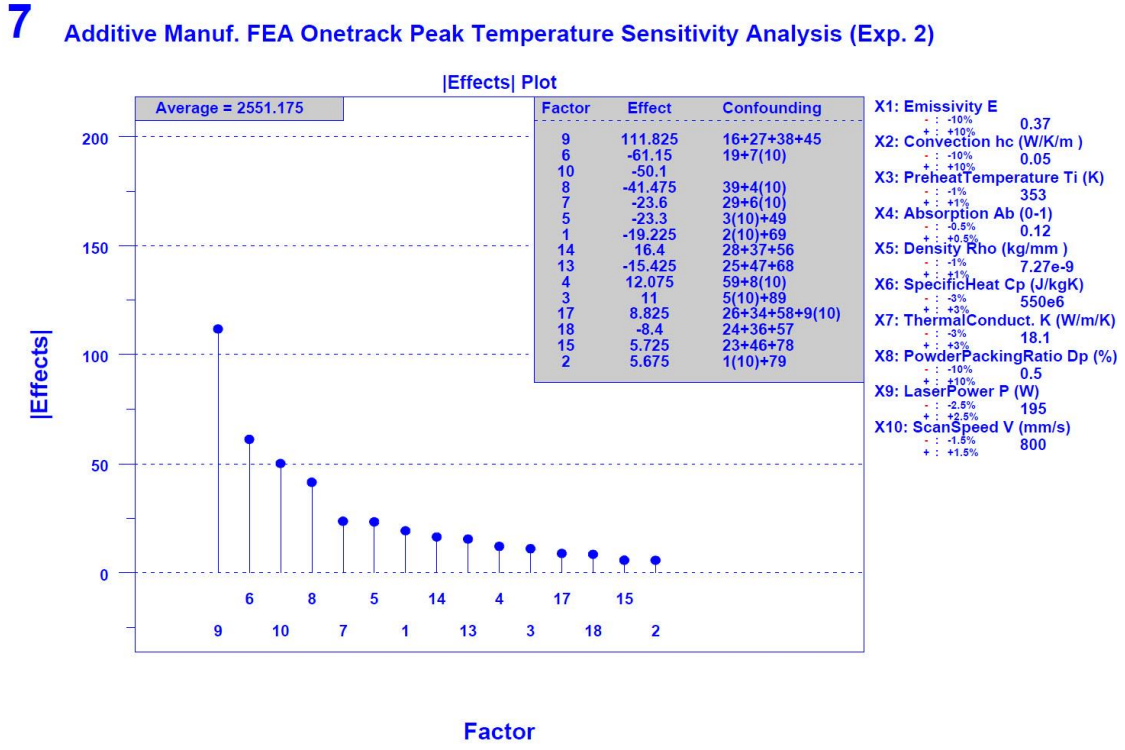

Figure 4: Ranking of effects plot of the 10-factor, 16-run 2-level, fractional factorial orthogonal DOE

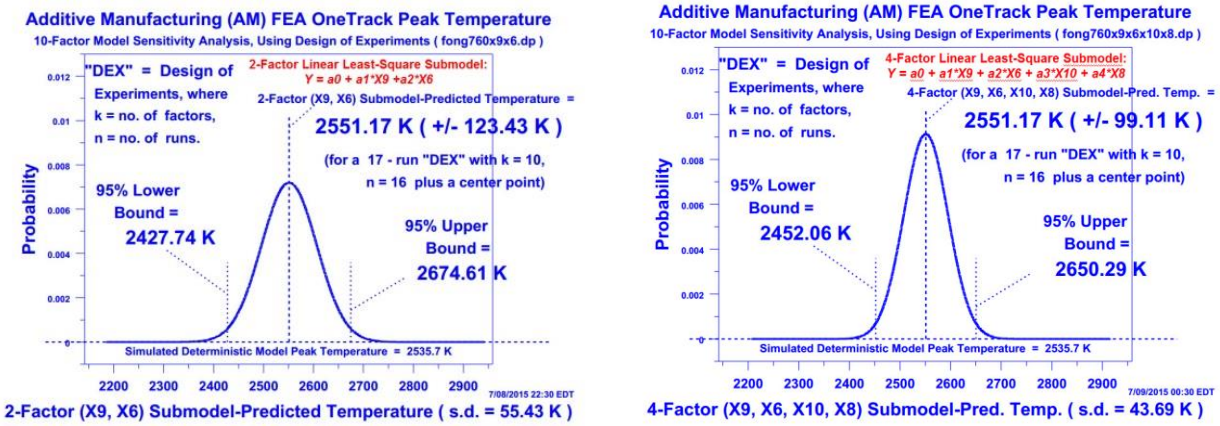

Figure 5: Uncertainty estimation based on (a) 2-Factor and (b) 4-Factor linear least-square submodel.

4. Concluding Remarks

We characterized FEA thermal modeling of a single track L-PBF process using a 10-factor, 16-run, 2-level, fractional factorial orthogonal design of experiments. We obtained the order of dominant factors affecting the IN625 single track peak temperature as (1) laser power, (2) specific heat, (3) laser scan speed, and (4) powder packing ratio; all of these factors affected the peak temperature by ≥ 2 %. Processing parameters (laser power and scanning speed) and material properties (specific heat and powder packing ratio) both impact the uncertainty quantification and the AM part quality.

Our computational design of experiments method provides an exploratory tool for examining a large number of factors and alternative modeling approaches, allowing us to determine which approaches can best predict AM process performance. The largest potential impact of this work is to determine what process parameters and material properties most affect the quality of an AM-manufactured part. This will allow AM process experts to concentrate their efforts on those factors that have the largest impact.

Acknowledgements

The authors gratefully acknowledge the valuable discussions on the modeling and DOE with Alkan Donmez and Richard E. Ricker from NIST, and IN625 thermal properties with Carelyn E. Campbell, William Boettinger, and Sudha Cheruvathur from NIST.

References

[1] EWI submitted to NIST, "Volume 1: Development and Measurement Analysis of Design Data for Laser Powder Bed Fusion Additive Manufacturing of Nickel Alloy 625 Final Technical Report", August 28, 2014. http://ewi.org/eto/wp-content/uploads/2015/04/70NANB12H264_Final_Tech_Report_EWI_53776GTH_Distribution_Vol_1.pdf

[2] Shiomi, M., Yoshidome, A., Abe, F., and Osakada, K., "Finite element analysis of melting and solidifying processes in laser rapid prototyping of metallic powders", International Journal of Machine Tools & Manufacture, 39, 237-252, 1999.

[3] Matsumoto, M., Shiomi, M., Osakada, K., and Abe, F., "Finite element analysis of single layer forming on metallic powder bed in rapid prototyping by selective laser processing", International Journal of Machine Tools & Manufacture, 42, 61–67, 2002.

[4] Ameer, K. I., Derby, B., and Withers, P. J., "Thermal and Residual Stress Modelling of the Selective Laser Sintering Process", Materials Research Society,758, 47-52, 2003.

[5] Kolossov, S., and Boillat, E., "3D FE simulation for temperature evolution in the selective laser sintering process", International Journal of Machine Tools and Manufacture, 44 (2-3),117-123, 2004.

[6] Patil, R. B., and Yadava, V., "Finite element analysis of temperature distribution in single metallic powder layer during metal laser sintering", International Journal of Machine Tools and Manufacture 47(7-8): 1069-1080, 2007.

[7] Roberts, I. A., Wang, C. J., Esterlein, R., Stanford, M., and Mynors, D. J., "A three-dimensional finite element analysis of the temperature field during laser melting of metal powders in additive layer manufacturing", International Journal of Machine Tools and Manufacture, Vol. 49 iss:12 pp. 916-923, 2009.

[8] Dong, L., Makradi, A., Ahzi, S., and Remond, Y., “Three-dimensional transient finite element analysis of the selective laser sintering process”, Journal of Materials Processing Technology, 209, 700–706, 2009.
[9] Zhang, D. Q., Cai, Q. Z., Liu, J. H., Zhang, L., and Li, R. D., "Select laser melting of W–Ni–Fe powders: simulation and experimental study", The International Journal of Advanced Manufacturing Technology, 51(5-8), 649-658, 2010.
[10] Li, C., Y. Wang, et al. "Three-dimensional finite element analysis of temperatures and stresses in wide-band laser surface melting processing", Materials & Design, 31(7): 3366-3373, 2010.
[11] Song, B., Dong, S., Lao, H., and Coddet, C., "Process parameter selection for selective laser melting of Ti6Al4V based on temperature distribution simulation and experimental sintering", The International Journal of Advanced Manufacturing Technology, 61(9-12): 967-974, 2012.
[12] Shuai, C., Feng, P., Gao, C., Zhou, Y., and Peng, S., "Simulation of dynamic temperature field during selective laser sintering of ceramic powder", Mathematical and Computer Modelling of Dynamical Systems, 19(1), 1-11, 2013.
[13] Yin, J., Zhu, H., Ke, W., Dai, C., and Zuo, D., "Simulation of temperature distribution in single metallic powder layer for laser micro-sintering", Computational Materials Science 53(1), 333-339, 2012.
[14] Hodge, N. E., Ferencz, R. M., and Solberg, J. M., “Implementation of a thermomechanical model for the simulation of selective laser melting”, Computational Mechanics, 54(1), 33-51, 2014.
[15] Abaqus, Theory and User’s manual, version 6.13, Dassault Systèmes Simulia Corp., Providence, RI., USA, 2013.
[16] Carslaw, H.S., and Jaeger, J.C., “Conduction of Heat in Solids”, Oxford University Press, Amen House, London E.C.4, 2005.
[17] Rombouts, M., Froyen, L., Gusarov, A. V., Bentefour, E. H., and Glorieux, C., “Photopyroelectric measurement of thermal conductivity of metallic powders”, Journal of Applied Physics, 97(2), 013534, 2005.
[18] Alkahari, M. R., Furumoto, T., Ueda, T., Hosokawa, A., Tanaka, R., and Abdul Aziz, M.S., “Thermal conductivity of metal powder and consolidated material fabricated via selective laser melting”, Key Engineering Materials, 523-524, 244-249, 2012.
[19] Childs, T., Hauser, C., and Badrossamay, M., “Selective laser sintering (melting) of stainless and tool steel powders: experiments and modelling, Proc Inst Mech Eng, Part B: Journal Engineering Manufacturing, 219(4), 339–57, 2005.
[20] TC Ni-based Superalloys Database, version 6; Thermo-Calc Software, Stockholm, Sweden, 2013.
[21] Thermo-Calc, version 3.1, Thermo-Calc software AB, Stockholm, Sweden, 2014.
[22] Mani, M., Lane, B., Alkan, M. A., Feng, S., Moylan, S. and Fesperman, R., “ Measurement science needs for real-time control of additive manufacturing powder bed fusion processes NISTIR 8036”, National Institute of Standards and Technology, 2015.
[23] Box, G. E. P., Hunter, H. G., and Hunter, J. S., Statistics for Experimenters: An introduction to design, data analysis, and model building, New York, Wiley, 1978.
[24] Filliben, J. J., and Heckert, N. A., DATAPLOT: A Statistical Data Analysis Software System, a public domain software released by NIST, Gaithersburg, MD 20899, http://www.itl.nist.gov/div898/software/dataplot.html, 2002.